OPEN ACCESS

University of BRISTOL

Showkat Ali, S. A., Szke, M., Azarpeyvand, M., & Ilário da Silva, C. R. (2016). Trailing Edge Bluntness Flow and Noise Control Using Porous Treatments. In 22nd AIAA/CEAS Aeroacoustics Conference. [AIAA 2016-2832] American Institute of Aeronautics and Astronautics Inc, AIAA. DOI: 10.2514/6.2016-2832

Peer reviewed version

Link to published version (if available):
10.2514/6.2016-2832

Link to publication record in Explore Bristol Research
PDF-document

This is the accepted author manuscript (AAM). The final published version (version of record) is available online via AIAA at http://dx.doi.org/10.2514/6.2016-2832. Please refer to any applicable terms of use of the publisher.

University of Bristol - Explore Bristol Research

General rights

This document is made available in accordance with publisher policies. Please cite only the published version using the reference above. Full terms of use are available:
http://www.bristol.ac.uk/pure/about/ebr-terms.html

Trailing Edge Bluntness Flow and Noise Control Using Porous Treatments

Syamir A. Showkat Ali*, Máté Szőke†, M. Azarpeyvand‡
Department of Mechanical Engineering, University of Bristol, BS8 1TR, UK
Carlos R. Ilário da Silva§
Embraer, São José dos Campos, 12227-901, Brazil

This paper is concerned with the noise generation mechanism from blunt trailing edges and the use of porous treatments as a mean to reduce the radiated noise and stabilizing the wake flow. Experiments have been carried out for flat plates with and without porous trailing edge for a wide range of Reynolds numbers. To gain a better understanding of the underlying physics of the noise generation mechanism and the effects of porous trailing edges, data has been collected for steady and unsteady aerodynamic forces, hot-wire measurements within the boundary layer and the wake region and the boundary layer surface pressure measurement. It has been seen that the use of porous material can significantly reduce the unsteady drag fluctuations, stabilize the boundary layer, lessen the surface pressure fluctuations on the surface and control the wake flow. Results have shown that the use of porous surfaces leads to an increase of the shear stresses in the inner turbulent boundary layer thickness but significant reduction of the energy content of the larger turbulent structure in the outer layer. It has also been observed that the use of porous material leads to the reduction of the turbulence level within the near wake region and significant elongation of the turbulent structures in both spanwise and streamwise directions.

Nomenclature

L_x	fore-body length
L_z	spanwise length
h	plate thickness
B	bluntness parameter
U_∞	free stream velocity
Re	Reynolds number
BR	blockage ratio
H	wind tunnel height
PPI	pores per inch
U	mean velocity
U_{rms}	root mean square velocity
δ	99% boundary layer thickness
δ^*	boundary displacement thickness
St	Strouhal number
L_{11}	longitudinal integral length scale
ϕ_{uu}	Power spectral density of velocity fluctuations
x, y, z	cartesian coordinates

*Ph.D Student, Department of Mechanical Engineering, ss14494@bristol.ac.uk
†Ph.D Student, Department of Mechanical Engineering, m.szoke@bristol.ac.uk
‡Senior Lecturer and Royal Academy of Engineering Research Fellow, Mechanical Engineering, m.azarpeyvand@bristol.ac.uk
§Technology Development Engineer, Embraer, São José dos Campos, Brazil carlos.ilario@embraer.com.br

I. Introduction

The blunt trailing edge bodies have been widely used for numerous aerodynamic applications, such as the flatback airfoils and the wind turbine blades. The blunt body is known to have superior lift characteristics and structural improvement, however the use of blunt trailing edges also results in structural vibration and increase of drag, which is due to the undesirable vortex shedding generated by the blunt trailing edge. Generally, passive control systems have been widely used for flow control and noise reduction purposes for airfoils, bluff and blunt bodies in many engineering applications. The passive control methods include serration,[1–5] O-rings,[6] dimple,[7] longitudinal groove,[8] splitter plate,[9,10] morphing,[11,12] porous material[13–29] and etc. The use of porous material for blunt bodies to improve their aerodynamic and aeroacoustic performance has been the subject of numerous experimental and numerical research studies over the previous decades.[17–29] The fluid movement through the permeable material is governed by the geometrical and mechanical properties of the porous material, namely, porosity, permeability, tortuosity, pore size and the properties of the fluid. The complex internal structure of the pores (voids) potentially controls all relevant physical and chemical properties as well being a medium of different transport processes. The use of porous material as a flow control method depends on the influence of the relationship between the porosity and permeability. To date, prior research in this area has shown that careful implementation of porous materials can lead to robust flow control, turbulence stabilization and significant noise reduction.[17–29]

Blunt trailing edge noise has been an important topic due to the wide range of engineering applications they feature in. Bearmen and Tombazis[17,18] in their study involving spanwise periodical protrusions at the blunt trailing edge profiles resulted into 34 % reduction of drag. This is related with the mitigation of vortex shedding which was identified with the advancement of three dimensional structures in the shear layer. Interest in blunt airfoil, also called "thick airfoil" in several studies have shown significant improvement in the lift performance for a wide range of Reynolds number applications. Standish and Van Dam[19] concludes that blunt airfoils generate steep adverse pressure gradients leading to the premature flow separation. This can be seen from the upper surface of the airfoil even with small perturbations which moves a portion of pressure recovery to the airfoil's wake. Hoerner and Borst[20] showed that blunt trailing edge on symmetric G-490 airfoil have significant increase in the maximum lift coefficient and maximum-thickness to chord ratio (t/c) using a constant chord Reynolds number of 500,000. Moreover, the impact of blunt trailing-edge airfoil sections for lower Reynolds number have been considered by Sato and Sunada.[21] They have tested five airfoil sections at three different Reynolds number (33,000, 66,000 and 99,000) for the aerodynamic forces and flow visualizations studies. The results indicates that at low Reynolds number, the total drag is reduced and the maximum lift had been increased. In addition, the maximum lift to drag ratio has increased and the linearity of the lift curve have improved. Besides that, Deshpande and Sharma[22] have investigated the vortex flows behind a segmented blunt trailing edge with different spanwise, resulting into suppression of the periodic von Kármán vortex shedding in the near wake behind the blunt body. A comprehensive experimental study on the vortex shedding control from a blunt trailing edge using plasma actuator in laminar boundary layer regime had been conducted by Nati *et al.*[23] using hot wire anemometry and high speed PIV. The results indicate the suppression of von Kármán vortex in the developing wake region where the analysis shows reduction in the vortex shedding frequency peak during steady plasma actuation by 10 dB.

Bruneau *et al.*[24] had numerically studied the use of porous interfaces on the blunt bodies in order to regularise the flow and reduce drag. Results had shown the capability of porous layer in reducing the pressure gradient near wake up to 67 % and considerable drag reduction up to 45 %. The effect of porous treatment on blunt trailing edge of a flat plate have been investigated by Bae *et al.*[25] The three-dimensional turbulent flow over the blunt trailing edge flat plate has been studied using incompressible large eddy simulation (LES) and linearized perturbed compressible equations (LPCE) with Reynolds number of 130,000 and M=0.06. It was found that the porous surface weakens the pressure fluctuations near the trailing edge for separate flow cases, which results in noticeable noise reduction of up to 10 dB over a wide range of frequency. The broadened tonal noise also have been reduced significantly up to 13 dB by breaking the wall pressure fluctuations space correlation length. Bae and Moon[26] have studied the effects of permeable material surfaces on turbulent noise generated by a blunt trailing edge of flat plate using LES on the domain rigid on LPCE, and the results have shown significant reduction of the broadband noise over a wide range of frequencies. Schulze and Sesterhenn[27] have studied the use of porous material for trailing edge noise control and developed a methodology to maximise the noise reduction by optimizing the porous material. Zhou *et al.*[28] developed a discrete adjoint-based optimization framework to obtain optimal distribution of porous material on trailing edge of a flat plate using an LES solver. The results obtained indicated that there is possibility of minimizing

the turbulence near the trailing edge and therefore controlling the noise generation at the trailing edge. In addition, Koh *et al.*[29] investigated the trailing edge noise reduction of a flat plate using LES and Acoustic Perturbation Equations (APE). The results showed that the porous surface changes the turbulence structures in the shear layer, reduces the sound pressure level up to 3-8 dB and influences the tone generation by significant reduction in the peak by 10 dB.

As reviewed above, the viability of using porous materials as a passive method to control the flow and weaken aero-acoustic type noise sources has been verified experimentally and numerically in several research works over the past decades. In some more recent research activities, it has been tried to further improve the effectiveness of such porous treatments by optimizing the shape and mechanical properties of the porous section, *i.e.* porosity and resistivity. In this paper, passive flow control method based on porous material for blunt trailing edge has been investigated. The experimental setup and wind- tunnel tests are described in Sec. II. The results and discussions are detailed in Sec. IV.

II. Measurement Setup

Experiments were performed with two different porous materials applied at the blunt trailing edge in the open jet wind tunnel of University of Bristol (UoB). The wind tunnel has a test section with 1 m diameter and with a test section length of 2 m. The maximum reliable speed which can be set is 30 m/s with a maximum turbulence intensity of 0.05 %. Measurements were performed using Force Balance, Hot-wire Anemometry, Particle Image Velocimetry (PIV) and also surface boundary layer pressure measurement.

A. Blunt trailing edge model design and configuration

The model of the blunt trailing edge flat plate rig is shown in Fig. 1. The plate has a fore-body length of $L_x = 350\ mm$ and spanwise length of 715 mm (L_z) and h =20 mm thickness. The corresponding aspect ratios of the flat plate are $AR_x = L_x/D = 17.5$ and $AR_z = L_z/D = 35.75$. The model in the open jet wind tunnel gives a blockage ratio of $BR = 1.8$ %, which clearly has negligible effect on any obtained results.[30] The flat plate has an elliptical leading edge in order to prevent flow separation at the beginning of the plate, and to help for the turbulent boundary layer to develop before the porous region.

Turbulent vortex shedding will occur at the trailing edge if the plate has a critical bluntness ratio. To ensure the presence of vortex shedding, the ratio of the trailing edge height and the boundary layer displacement thickness must obey[31]

$$B = \frac{h}{\delta^*} > 0.3, \tag{1}$$

where B is the bluntness parameter, h is the model base height and δ^* is the boundary layer displacement thickness at the trailing edge. The ratio of h/δ^* can be determined by considering the flow over a smooth flat plate using empirical formula.[32] Based on the flow velocity of U_∞=20 m/s at Reynolds number $Re_{L_x} = 4.6 \cdot 10^5$, the boundary layer displacement thickness is approximately 1.1 mm. Hence, the ratio of bluntness parameter is approximately 18.2, which is significantly larger than the 0.3. In order to reach a well-developed turbulent flow before the porous section, a 25 mm wide sand trip was applied just aft the leading edge with a thickness of approximately 0.6 mm and grit roughness of 80. The trip was placed on both sides of the plate. The porous section is placed at the trailing edge with a width (L_{px}) and length (L_{pz}) of 50 mm and 500 mm, respectively, see Fig. 1. Two different porous materials were used with 25 and 80 pores per inch (PPI), which were made of aluminium, see Fig. 2. To ensure two dimensional flow over the span rectangular side-plates (425 mm x 80 mm) with sharpened leading edges with an angle of 20° were mounted on the rig. The side-plates were installed approximately $1.25h$ from the leading edge and $2.5h$ from the trailing edge. Figure 2 shows the rig installed in the wind tunnel.

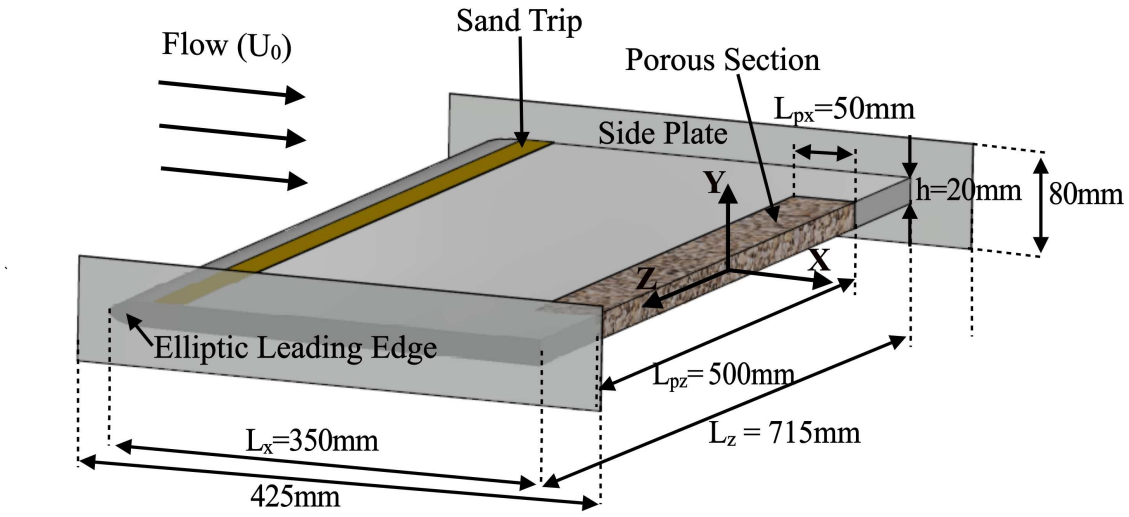

Figure 1: Flat plate blunt trailing edge schematic with major dimensions and the coordinate axis

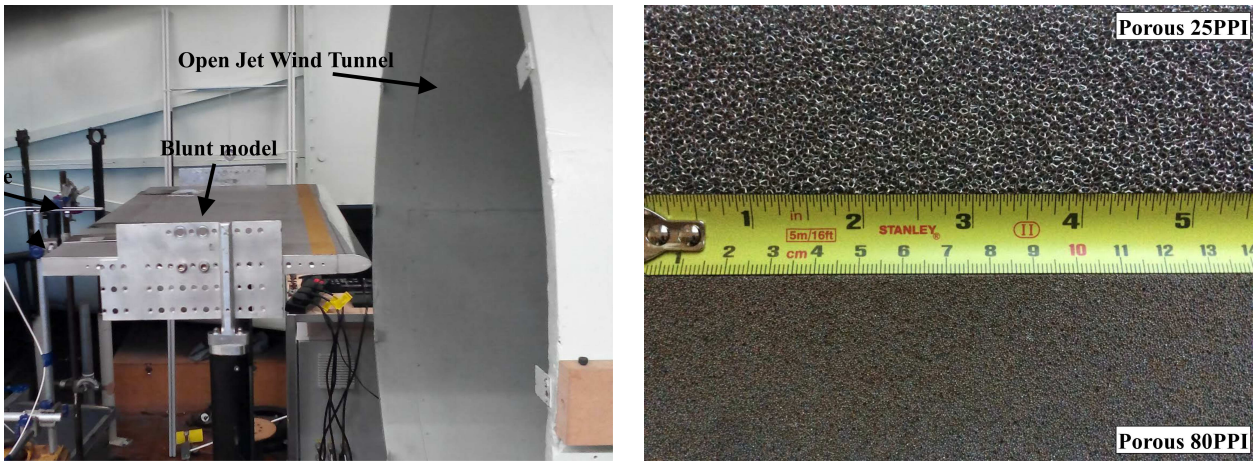

Figure 2: (a) The rig in the open jet tunnel with the single hot-wire probe (without side plates) (b) a picture of the applied porous materials

B. Force Balance Measurement Setup

All steady and unsteady aerodynamic measurements were performed in the open jet wind tunnel of the University of Bristol. The drag force measurements were collected using a force plate unit. The rig was mounted on a set of steel extension arms which had symmetrical tear drop shape to minimise any drag generated on them. The extension arms were fixed on the AMTI OR6-7-2000 force plate, which was load tested prior to the experiment. The generated voltage signal from the force plate passed through an AMTI MSA-6 strain gauge amplifier. The final data from this unit was captured using a LabView system. The measurement was performed for 30 seconds at each velocity with a sampling frequency of 45 Hz. Measurements were performed from 6 m/s to 26 m/s wind speed with 2 m/s increments. The speeds were set such that all data was recorded once the deviation of the velocity was 0.2 m/s or less. To ascertain the repeatability of the measurements, repeated tests were conducted and the uncertainty was found to be less than 1 % different from each other.

C. Hot-wire Anemometry Setup

To measure the turbulent properties of the flow, hot-wire anemometry was used. The flow measurements were carried out using single and cross hot-wire probes. The single hot-wire probes were Dantec 55P16 type with a platinum-plated tungsten wire of 5 μm diameter and 1.25 mm length. The cross hot-wire (X-wire) probe was a Dantec 55P51 type sensor with 5μm diameter and 3 mm length platinum-plated tungsten wires. The probes were operated by a Dantec StramlinePro frame which has two CTA91C10 modules. The applied overheat ratio was 1.8.[33] The signal was low pass filtered by the StreamlinePro frame with a corner frequency of 30 kHz before it was A/D converted. The data was acquired by a National Instrument 9215 type device, with a sampling frequency of to 40 kHz. The signals of the hot-wires were measured for 15 seconds at each location.

The calibration of the wires were performed using a Dantec 54H10 type calibrator. The calibration was employed by fitting a fourth order polynomial on the two known speeds. The X-wire probe was also calibrated using directional calibration to obtain the pitch and yaw coefficients on the same calibrator unit. The calibration process was performed before and after each measurement, and the polynomial constants were averaged prior to post processing of the results. The error analysis of the velocity values obtained by the use of the hot-wire probes was performed based on the manufacturers description.[33] Based on the description given by the manufacturer, the typical error of the measured velocity given by the single wire is less than 0.5 %. The uncertainty derived from the measured velocity signals were found to be within 1 %.

The hot-wire probe was installed on a traverse system. The system can cover 300 mm times 300 mm in two perpendicular directions. The system consists of two ThorLabs LTS300M stages, which typical minimum positioning accuracy is 5 μm.

D. Surface Pressure Measurement Setup

FG-23329-P07 miniature microphones are used for the measurement of the unsteady boundary layer surface pressure fluctuations. The microphones dimensions are of 2.5 mm diameter and height with 0.8 mm of circular sensing area. The use of this microphone was convinced to be reliable for trailing edge turbulent boundary layer measurement.[34,35] The trailing edge plate was instrumented with 11 microphones under a pinhole mask of 0.4 mm diameter in order to compensate the large discontinuities[36] of the pressure attenuation at the wall interfered with the turbulent field. Hence, a small-sized pinhole microphones sensing area can minimize the attenuation of pressure fluctuations and eliminate the errors presence in the wall pressure spectrum at high frequencies.[37,38] The microphones were installed inside the plate parallel (horizontally) to the surface and were arranged in the form of L-shaped array on the surface in the streamwise and spanwise directions. The microphones located in the spanwise direction will be used for calculation of the spanwise length scale of flow structures, whereas the microphones employed in the streamwise direction provide the information on the turbulent eddies convection velocity. Prior to this research, the unsteady boundary layer surface pressure fluctuations test was conducted using the microphones in the streamwise direction. The detailed arrangement of the miniature microphones on the detachable trailing edge is shown in Fig. 3 and their locations are summarized in Table 1.

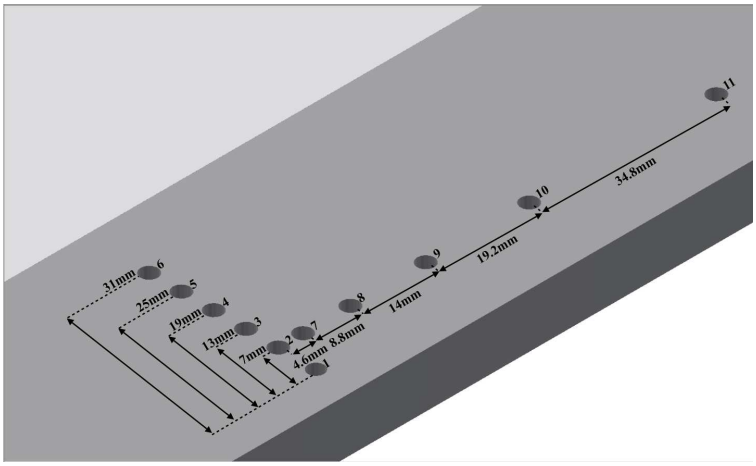

Figure 3: Distribution of microphones array in spanwise and streamwise directions

Table 1: Positions of pinholes microphones on the trailing edge

Position	**Microphones Number**	**Distance from Trailing Edge** (mm)	**Distance from Mid Span** (mm)
Streamwise	1, 2, 3, 4, 5, 6	7, 14, 20, 26, 32, 38	0.0
Spanwise	7, 8, 9, 10, 11	14	4.6, 13.4, 27.4, 46.6, 81.4

The spanwise pinhole microphones were arranged in a way to obtain a smooth distribution of potential function of turbulent properties near the trailing edge. The distance between the microphones has to be diverse and must not be small in order not to be affected by the scattering process of the pressure field at the trailing edge. The minimum sensor distance to avoid the scattering effects is approximately $\lambda_h/2$, where λ_h is the convected hydrodynamic wavelength of interest ($\lambda_h = U_c/f$).[39,40] Based on this specification, the spanwise microphones were placed 14 mm upstream of the trailing edge. The minimum and maximum distance of the pinhole microphone in spanwise direction is 4.6 mm and 81.4 mm, respectively. In contrast, uniform distribution of pinhole microphones was employed in the streamwise direction from microphone 2-6.

III. Data Analysis and Post Processing

The mean and root mean square velocities can be obtained from the velocity time history, as:

$$U = \frac{1}{N}\sum_{i=1}^{N} U_i, \tag{2}$$

and

$$U_{rms} = \sqrt{\frac{1}{N}\sum_{i=1}^{N}(U_i - U)^2}, \tag{3}$$

where N is the total number of velocity samples in time and U is denoted as the mean velocity.

The boundary layer thickness δ corresponds to the location where the velocity reaches 99 % of the free stream velocity U_∞. The boundary layer displacement thickness δ^* is defined in Eq. (4).

$$\delta^* = \int_{y=0}^{\delta} (1 - \frac{U(y)}{U_\infty})\mathrm{d}y, \tag{4}$$

where the integration was performed using the trapezoidal numerical integration method.

In order to calculate the the Reynold stresses, two simultaneous time series is needed at each location. The Reynolds stresses can be indicated as a tensor:

$$\tau_{ij} = -\rho\overline{u_i' u_j'}, \tag{5}$$

where ρ is the fluid density, $\overline{u_i' u_j'}$ express the velocity correlation of the momentum flux in the direction across a plane perpendicular to the coordinate direction. Average stress is attained from the turbulent fluctuating components as:

$$U_i = U + u_i', \tag{6}$$

Using the velocity data collected from the cross-wire probes, these can be calculated as:

$$-\overline{u'u'} = \frac{1}{N}\sum_{i=1}^{N}(U_i - U)(U_i - U)\,, \tag{7}$$

$$-\overline{v'v'} = \frac{1}{N}\sum_{i=1}^{N}(V_i - V)(V_i - V)\,, \tag{8}$$

$$-\overline{u'v'} = \frac{1}{N}\sum_{i=1}^{N}(U_i - U)(V_i - V)\,, \tag{9}$$

The Strouhal number based on the bluntness trailing edge thickness (h), and the free stream velocity (U_∞) is defined as;

$$St = \frac{fh}{U_\infty}. \tag{10}$$

To identify the pattern of turbulent structures in space, two point correlation function of the velocity is used:

$$R_{ii}(r) = \frac{< u_i'(x_i, t)u_i'(x_i + r, t) >}{< (u_i')^2 >}, \tag{11}$$

where u_i' is the fluctuating velocity in streamwise direction and r is the distance between measurement locations.

For the better understanding of the turbulent structures within the boundary layer and wake, it is important to study the integral length scale (L_{ij}). In this study, the integral length scale is obtained using the two-point velocity correlation function as:

$$L_{11}(x,t) \equiv \frac{1}{R_{11}(0,x,t)}\int_0^\infty R_{11}(\mathbf{e}_1 r, x, t)\mathrm{d}r, \tag{12}$$

where $\mathbf{e}_1$ is the unit vector in the x_1-coordinate direction, r is the distance between the two measuring points and R_{ij} is the two-point one-time autocovariance.[41]

To resolve the energy signal in the frequency domain, Welch's power spectral density of velocity fluctuations (ϕ_{uu}) has been calculated based on the time history data velocity fluctuations. The calculation was performed in Matlab using Hamming windowing, with 50 % overlapping and segmenting. The frequency resolution (Δf) was set to 64 Hz from which defined a sample length for a whole wavelength of this frequency. This wavelength was equal to 1/5 of the window length used in the windowing process.

IV. Results and Discussion

A. Steady Drag Coefficient

The steady and unsteady aerodynamic force measurement of the blunt TE flat plate with solid and porous trailing edges are presented and explained in this subsection. The experiments covered a wide range of plate length (L_x) based Reynolds numbers: $Re_{L_x} = 1.3 \cdot 10^5$ to $5.8 \cdot 10^5$, corresponding to the flow velocity of U_∞=6 m/s to U_∞=26 m/s. The results presented in Fig. 4, show the drag coefficient (C_D) of the plate against the Reynolds number, for the solid and porous TEs. It can be seen that all the porous treatments have

reduced the C_D. Notably, there is a sudden sharp drop in C_D for all cases at the range up to $Re_{L_x} = 3 \cdot 10^5$. After this point, the drag coefficient gradually decreases over the lower critical region ($> Re_{L_x} = 3 \cdot 10^5$) of the plate. The 25 PPI porous material has the largest reduction in C_D, roughly 16 % followed by porous media with 80 PPI porosity compared to the solid case. Also, the trend shown by the solid and porous with 80 PPI cases were almost identical. This behaviour can be explained by the fact that it takes more space/time for the flow to penetrate into the 80 PPI material, and therefore the porous material with high PPI, lower permeability behaves more similar to the solid case.

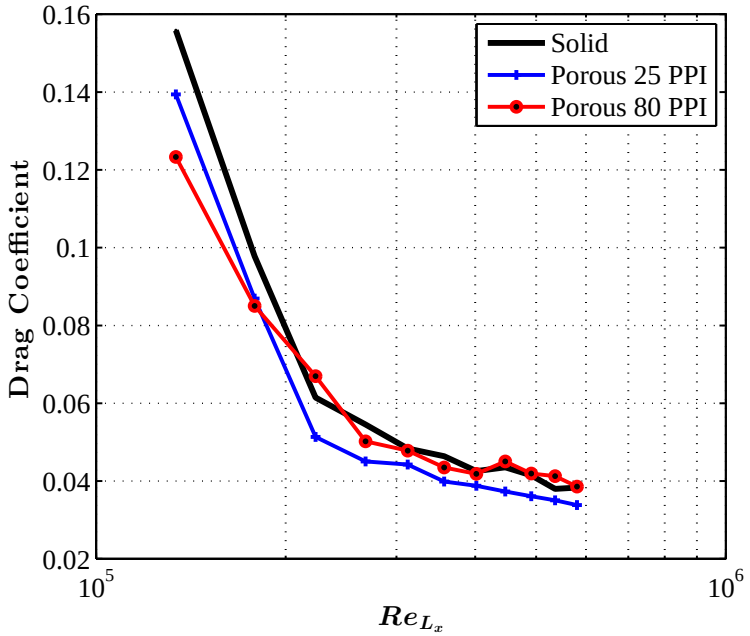

Figure 4: The measured drag coefficients for the different cases: *black line: solid; blue line: porous 25 PPI; red line: porous 80 PPI.*

B. Boundary Layer Analysis

1. *Velocity Profile and Their Energy Content*

The behaviour of the boundary layer upstream of the blunt trailing edge was studied for different cases. The measurement is conducted at zero angle of attack and the free-stream flow velocity was set to U_∞=20 m/s. The detailed locations of the measurements are shown in Table 2 and in Fig. 5 . The locations are denoted by BL_1, BL_2, BL_3 and BL_4. The distance between two neighbouring lines corresponds to $1/3L_{px}$. The hot-wire probe has been traversed and the data has been collected between $y \approx 0$ mm and $y = 50$ mm at 35 points above the plate for each line.

Table 2: Measurement locations in the boundary layer and wake region

Measurement Regions	**Measurement Locations**	**Upstream distance from TE** (mm)	**Downstream distance from TE** (mm)
Boundary Layer Region	BL_4, BL_3, BL_2, BL_1	1.0, 17.7, 34.3, 51.0	-
Wake Region	W_1, W_2, W_3, W_4, W_5, W_6	-	2, 10, 20, 40, 60, 100

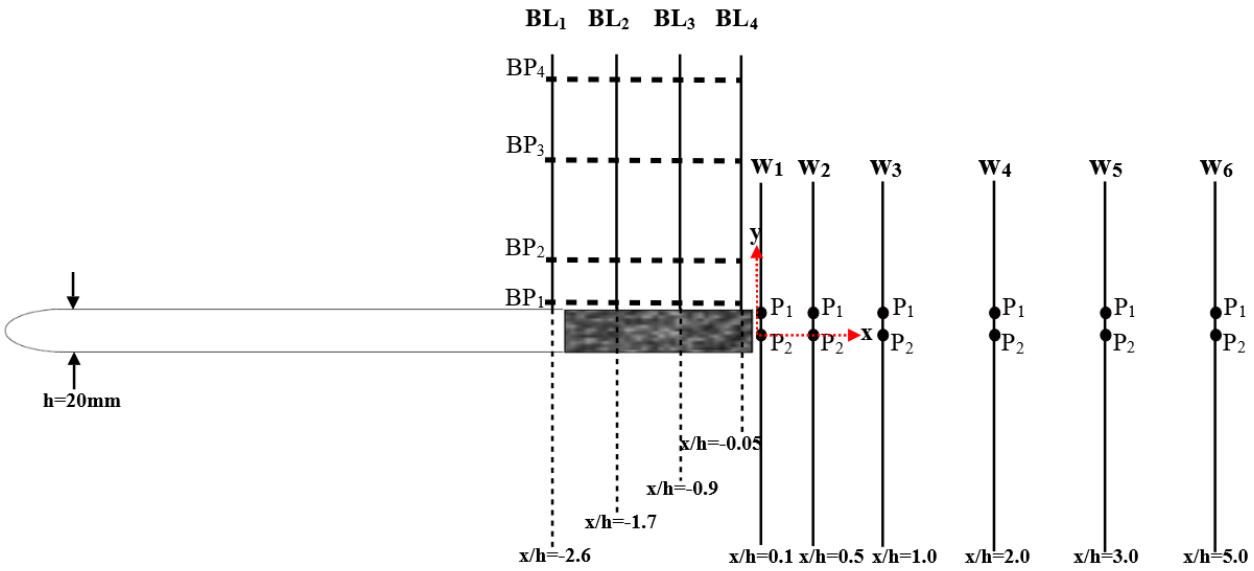

Figure 5: The schematic of the blunt trailing edge rig and the positions of the hot-wire measurements

Figure 6 presents the mean and rms boundary layer velocity profiles along the BL lines shown in Fig. 5. The y axis of the boundary layer profile have been normalized by the boundary layer thickness at BL_1. Note that at BL_1, the velocity of fluid goes to zero at the boundary in which that the no-slip condition is still valid at the wall and is not the same in the case of porous boundary. The velocity profile results show that there is an increase in the velocity gradient at the wall from BL_1 to BL_4 and the boundary layer thickness found to be decreasing from BL_2 to BL_4. This implies that favorable or negative pressure gradient occurs near the TE which tend to accelerate the flow.[42] All of the boundary layer profile downstream from BL_1 change, and they differ from the fully developed turbulent boundary layer profile because over an infinitely long flat plate, as the bluntness causes significant velocity overshoot in the vicinity of the trailing edge. By comparing the boundary layer profiles, it is noticed that the profiles are quite similar in the first two locations (BL_1 and BL_2). Results have shown that the porous materials decrease the bluntness acceleration, *i.e.* the red and blue profiles show lower velocities. The 25 PPI material reduces the acceleration the most, which is well visible at the BL_4 location.

The presented RMS velocity profiles show reduction when the porous material was applied at the trailing edge. This becomes clearly visible at x=17.7mm (BL_3) and x=1mm (BL_4), upstream of the trailing edge. However, there is an increase in the RMS velocity magnitude near the wall especially for the case of porous 25 PPI at both BL_3 and BL_4. This means that there is an increase in the energy content near the wall, which is believed to have been caused due to viscous friction effect taken place at the porous surface. However, results show that the overall energy content in the boundary layer is significantly reduced by both porous materials, but especially by the 25 PPI one.

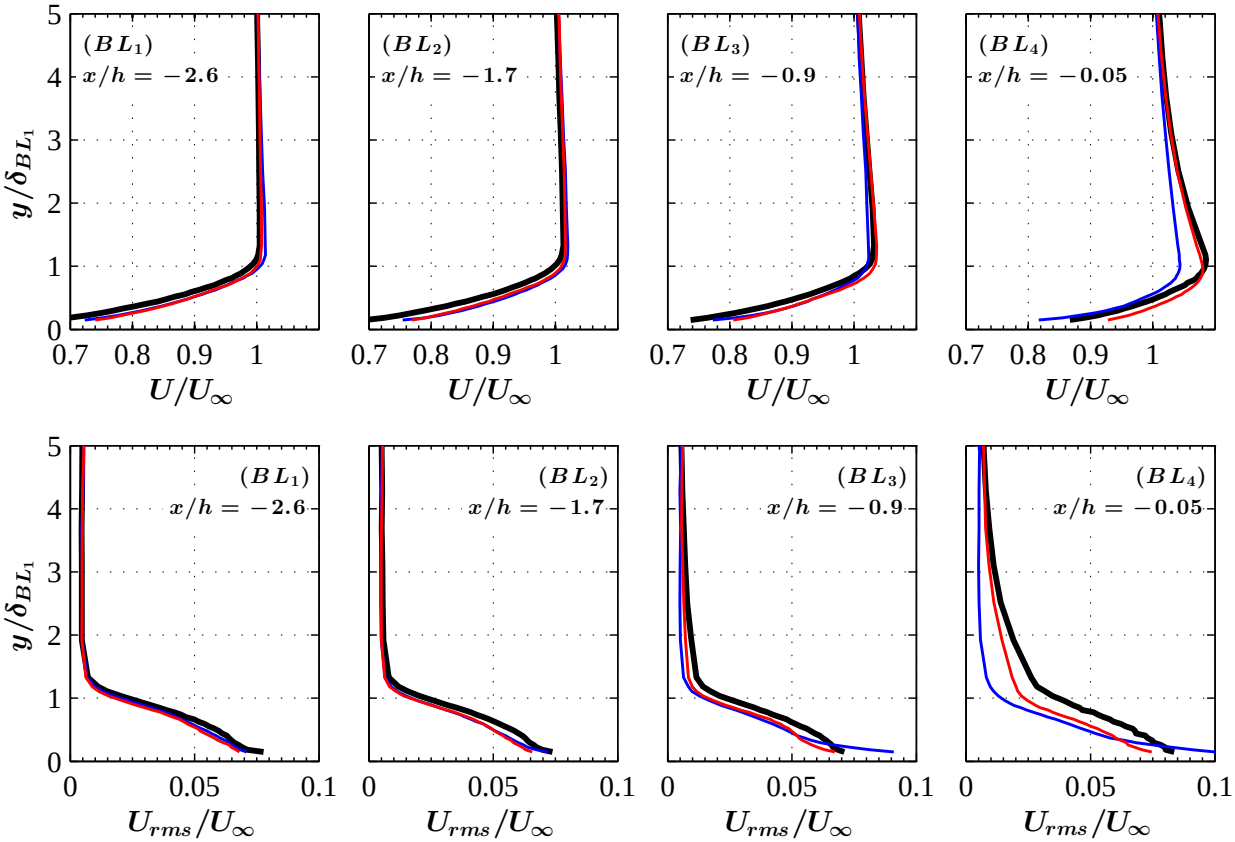

Figure 6: Boundary layer mean and RMS velocity profiles at different streamwise locations over the blunt trailing edge flat plate model. *black line: solid; blue line: porous 25 PPI; red line: porous 80 PPI.*

2. *Velocity Power Spectra in the Boundary Layer*

The location of the dominant turbulent structures within the boundary layer and their frequency energy content can be studied using the velocity power spectrum (ϕ_{uu}). Figure 7 presents the velocity power spectral density as a function of the Strouhal number at different axial locations upstream of the TE and provides comparison between the three investigated cases. The spectra at BP_{1-3}, BL_{1-4} shows the near wall region, of which BP_1 correspond to the point near the surface. The spectra at BP_4, BL_{1-4}, on the other hand, show the outer layer of the boundary layer.

In the vicinity of the wall, the porous material especially in the case of 25 PPI causes an increase in the energy content over the whole Strouhal range, which is in agreement with the RMS velocity profiles in Fig. 6. The investigated spectra at BP_3, BL_{1-4} corresponds to the inner edge of the turbulent boundary layer edge. At this location, it is clearly visible that the energy content of the porous cases have been reduced significantly. However, in the outer layer (BP_4, BL_{1-4}), all the porous materials experience an increase in the energy content compared to the solid TE, which appear to be due to the detached eddies from the TE wall. The inner layer is predominantly composed of wall attached eddies of quasi-streamwise vortices. The characteristics between attached and detached eddies are given by Perry and Marušic.[43] Consequently, these eddies in the inner layer which interacts on the TE wall will have a very significant effect on its structure. The energy reduction observed in the case of porous TE is believed to be the result of eddies break-up in the porous media. The tonal peaks are well visible for solid and porous 80 PPI in the vicinity of the TE at BL_{3-4}.

The tonal peak occurs at $St \approx 0.21$, which corresponds to the vortex shedding frequency as expected. The peaks vanish in the case of the 25 PPI porous material apart from the BP_4, BL_4 (upper right plot) case. This is believed to be due to the fact that this material has a flow stabilizing effect in the near wake regions.

This will be further discussed in Sec. D 3. One can infer from the results that the two porous materials have very different effects on the tonal peaks, as well as the broadband content

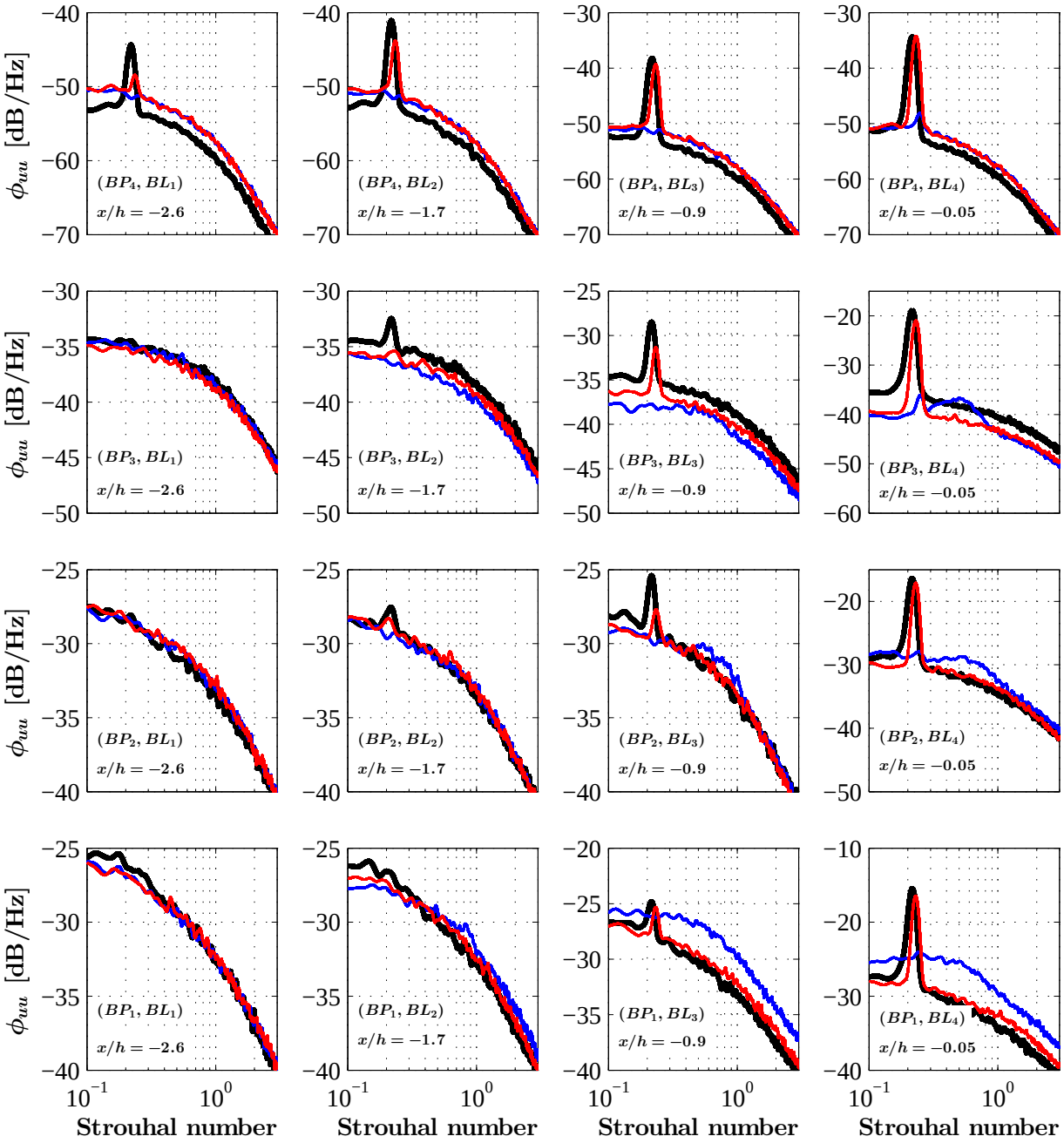

Figure 7: The power spectral density at different locations in the boundary layer. *black line: solid; blue line: porous 25 PPI; red line: porous 80 PPI*

C. Surface Pressure Measurement

1. *Velocity-Pressure Correlation ($R_{u'p'}$ and $R_{v'p'}$) in the Boundary Layer*

In characterizing the noise generated from the trailing edge, it is essential to examine both the fluid field and the pressure exerted on the surface. The correlation studies between the velocity field within the BL and the surface pressure fluctuations were conducted in order to identify the characteristics of the coherent turbulent structure and the statistical properties of fluctuations in space and phase relation. The flow velocity was set to U_∞=20 m/s and the measurements were taken at four locations above the microphones numbered 1,2,4 and 6, as shown in Fig. 3. The locations are denoted by BL_{m1}, BL_{m2}, BL_{m4} and BL_{m6}. Cross-wire probe has been used and the data has been collected between $y \approx 0$ mm and $y = 50$ mm at 49 locations above each microphone.

Figure 8 presents the velocity-pressure $R_{u'p'}$ and $R_{v'p'}$ correlation profiles within the BL at different distances from the trailing edge. The y axis of the velocity-pressure correlation plots have been normalized by the boundary layer thickness at BL_1 (Fig. 5). It is noticed that the values of correlation coefficient clearly increase in the negative scale downstream of the trailing edge for all porous cases in both $R_{u'p'}$ and $R_{v'p'}$ correlation profiles at the locations near to the wall. As for the solid case, the $R_{u'p'}$ correlation is highly concentrated in the negative region at the position closer to the wall between BL_{m2} to BL_{m6}, and positively correlated at BL_{m1}. The positive correlation can also be seen for the case of porous 80 PPI at BL_{m1} and BL_{m2}, however this trend does not appear in the case of porous 25 PPI. On the contrary, the $R_{v'p'}$ value is negatively correlated for all cases, where porous 80 PPI displays higher correlation value compared to others.

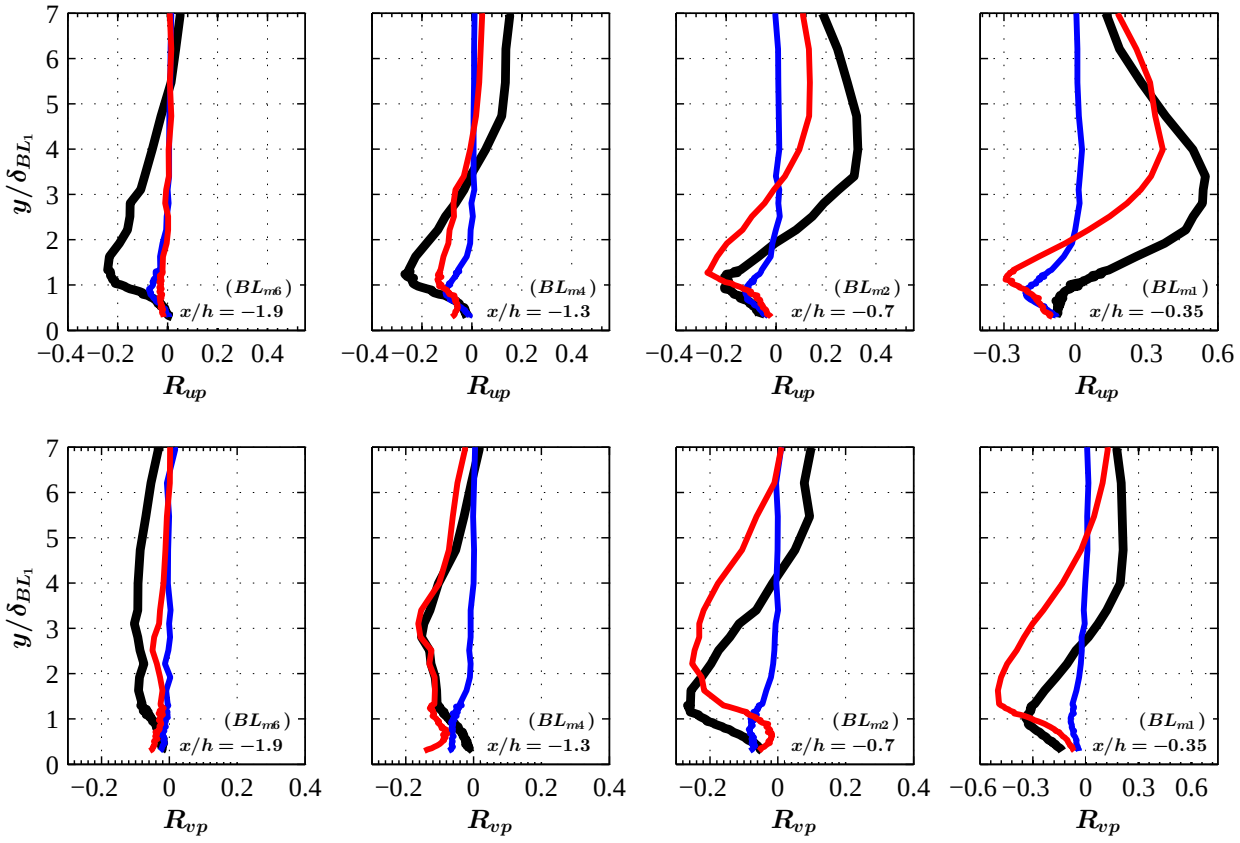

Figure 8: Velocity-Pressure Correlation, $R_{u'p'}$ (upper row) and $R_{v'p'}$ (lower row) in the boundary layer correlation profiles at different streamwise locations over the blunt trailing edge. *black line: solid; blue line: porous 25 PPI; red line: porous 80 PPI.*

The negative correlation in Fig. 8 indicates that an increase in the velocity or pressure fluctuating signal reliably predicts a decrease in the other one. In other words, the negative correlation demonstrate that the fluctuating velocity components ($u^{'}$, $v^{'}$) and $p^{'}$ are out of phase in the flow. G.I. Taylor[44] interpret that the negative correlation as the consequence of the outer rough boundary layer edge on the external flow. Due to the continuity of the flow, the boundary layer will thicken as the effect of strong downstream disturbance which principally slowing up of the boundary layer at any moment. A bump is present to the outer potential flow, and the flow will accelerate up in passing over the bump. Hence, this two consecutive effects will result in opposite phase and therefore the negative correlation occurs. Thus, from the boundary layer velocity profile results obtained previously, the flow direction downstream the trailing edge tend to accelerate the flow which compromise the context of the resulting negative correlation. This peculiar result have not been noted in any of the earlier studies.

D. Hot-wire Measurements in the Wake

To better understand the effect of porous material on the aerodynamic performance and the flow field, the mean velocity and Reynolds shear stresses profiles are presented in this section. Further discussion on the frequency response for selected measurement points and energy content of each cases are also presented here.

1. Wake Velocity Profile

Measurements have been performed using cross hot-wire probes in the wake at the Reynolds number of ($Re_{L_x} = 4.6 \cdot 10^5$), corresponding to the flow velocity of U_∞=20 m/s. The measurement locations can be seen in Fig. 5, namely $x/h = 0.1$, $x/h = 0.5$, $x/h = 1.0$, $x/h = 2.0$, $x/h = 3.0$ and $x/h = 5.0$ downstream of the trailing edge. A total number of 66 points were captured over 0<y<300mm for both U and V component in each line of measurements using cross wire probe.

Figure 9 shows the U and V velocity profiles at these locations. It is clearly visible that the porous treatment significantly changes the wake profiles in both x and y directions. The 25 PPI material significantly reduces the magnitude of U velocity in the wake, while the 80 PPI is closer to the solid case, but still gives a reasonable reduction. The U velocity profiles show that the porous treatment delays the formation of vortex shedding in the wake, *i.e.* near-wake stabilization. Generally, it can be seen that the momentum deficit in the porous cases especially for the case of porous 25 PPI is larger than that of the solid case at all downstream locations. The large deficit in momentum for porous TE cases in the wake is the result of the acceleration flow from the blunt TE which cause larger pressure gradient in the wake. It is apparent that the difference between the solid and porous results decreases at downstream locations. On the other hand, the gradient of the U velocity component still remains high for the case of porous 25 PPI as the vortices are broken into smaller eddies or have been suppressed by the porous plate. The effect of porous TE restraint the entrainment of the high momentum fluid from the free-stream into the wake field. This causes lower momentum transfer in the wake and results in large velocity deficit in the case of porous TE. Lim and Lee[45] showed that the large velocity deficit in the wake region promotes lower drag force in the case of bluff body. This evidence is in agreement with the results obtained in Fig. 4. The V velocity component shows different behaviour than U. The V velocity is accelerated in the near wake up to $x/h = 2.0$; where the velocity is positive for $y > 0$ and negative for $y < 0$, which cause the free-stream flow directed away from the TE centerline. In contrast, at $x/h = 3.0$; the velocity phase changes and the free-stream flow is directed towards the centerline and the V velocity became significantly smaller and almost identical for all cases at $x/h = 5.0$.

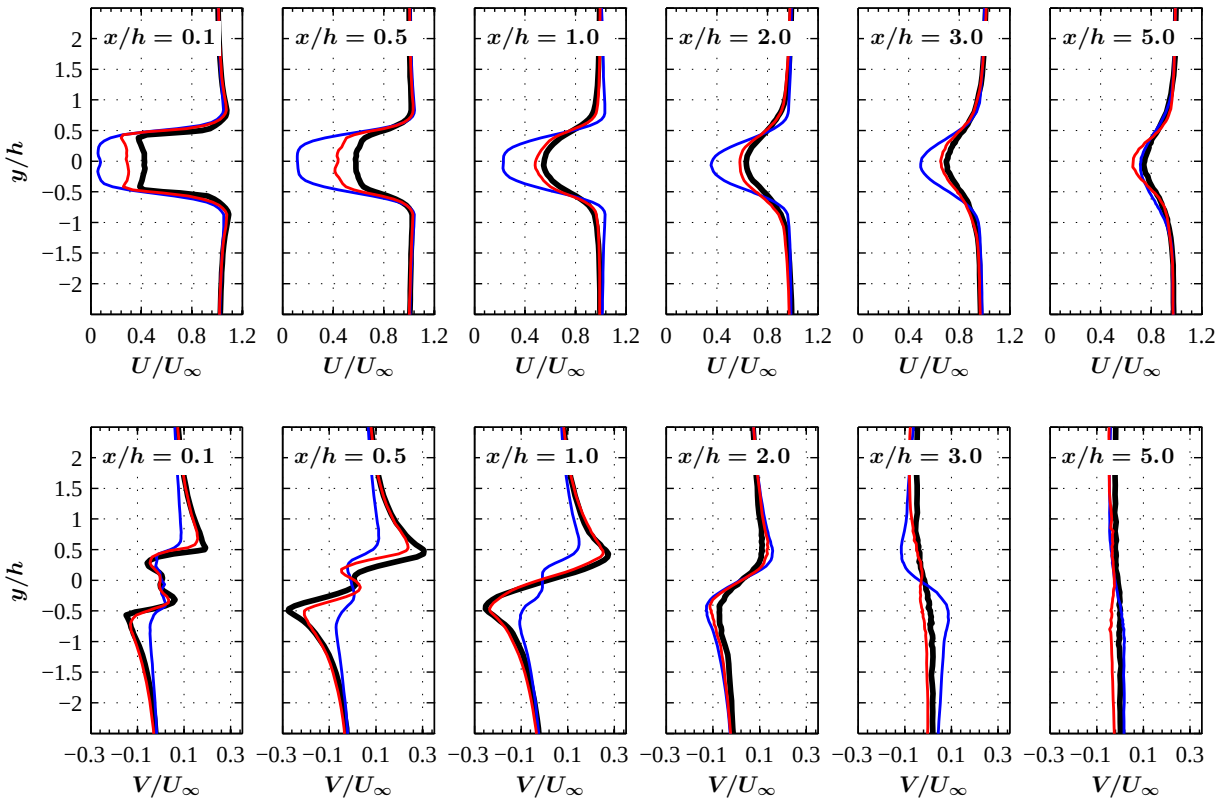

Figure 9: Mean U and V velocity components in the wake of the blunt trailing edge. *Black line: Solid; Blue line: Porous 25 PPI; Red line: Porous 80 PPI.*

2. *Reynold Stresses Velocity Profile*

Figure 10 presents the Reynold Stresses results: the eddy normal stress($-\overline{u'u'}/U_\infty^2$, $-\overline{v'v'}/U_\infty^2$) and the eddy shearing stress component ($-\overline{u'v'}/U_\infty^2$) within the wake at x/h= 0.1, 0.5, 1.0, 2.0, 3.0, and 5.0. It is clear from the figure distribution that the Reynold Stresses are symmetrical along the wake centerline for all cases. Both the eddy normal stress components $-\overline{u'u'}/U_\infty^2$, $-\overline{v'v'}/U_\infty^2$ of the porous values were reduced at all locations. Similarly as before, the 25 PPI shows larger and 80 PPI showed lesser reduction, but unlike in the mean velocity profiles, these profile show reduction consistently. The peaks in $-\overline{u'u'}/U_\infty^2$ and $-\overline{v'v'}/U_\infty^2$ are starting from the same location: $y/h \approx \pm 0.5$, *i.e.* at the edges, but afterwards the distance between the peaks for the different cases are different. The 80 PPI remains close to solid case, but still the peaks in that case get closer to each other. It also reduced the width of the peak in $-\overline{v'v'}$ at x/h=3.0 and 5.0. Porous 25 PPI has reduced the velocity fluctuations significantly at all locations, however the $-\overline{v'v'}$ for porous 80 PPI tend to increase at the last two locations.

Results have shown that there is noticeable difference between the magnitude of the $-\overline{u'u'}$ and $-\overline{v'v'}$ eddy normal stress terms. The $-\overline{v'v'}$ becomes twice as large as the $-\overline{u'u'}$ at the last four locations. The increase in the v fluctuation indicates the presence of large swirling turbulent structures, *i.e.* the formation of vortex shedding.[46] Also, this suggests that the turbulence shows anisotropy at these locations due to strong vortex shedding. It can therefore be concluded that the effect of porous treatment on the trailing edge was to break-down the large flow structure in the near wake which was signified by the reduction in the velocity fluctuations in the wake region particularly for the case of porous 25 PPI.

The last plot in Fig. 10 illustrates the Reynold Shear Stress ($-\overline{u'v'}/U_\infty^2$), which describes the transport of momentum due to the turbulent fluctuations in the flow. The figure at each location displays a symmetrical distribution of shear stress along the wake centerline. The region with strong local production of turbulence can be seen in the case of solid TE in the near wake, which its shear stress gradient is larger relative to the porous cases. It is clear that the shear stress is reduced significantly at x/h=0.1 to x/h=2.0 due to the

larger momentum deficit in the case of 25 PPI. Also, the lower peaks in the case of 25 PPI compared to the solid TE is due to the elongation of the wake region and the suppression of vortex shedding. In contrast, the distribution of $-\overline{u'v'}$ obtained at x/h=3.0 and x/h=5.0 shows a slight increase in the peak concentration in the porous 25 PPI case. It is also clear that the fluctuations of the velocity components have negligible values in the porous 80 PPI case at the last two locations indicating that the vortices are removed.

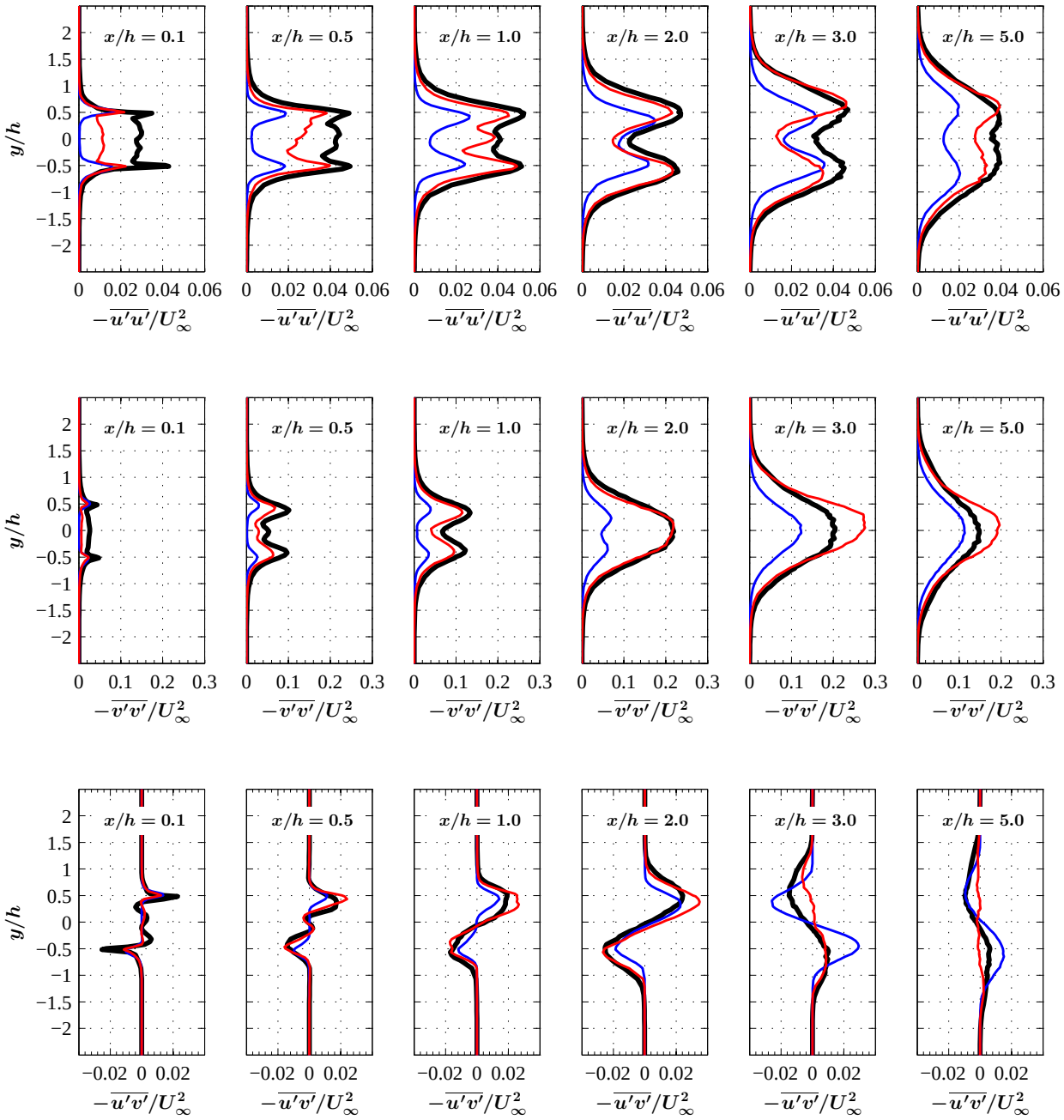

Figure 10: Reynolds stresses components within the wake. *Black line: Solid; Blue line: Porous 25 PPI; Red line: Porous 80 PPI.*

3. *Power Spectra of the Wake Velocities*

The strength of the eddies in the wake can be investigated with the help of the velocity power spectra. These variables were plotted in Fig. 11 at several wake locations downstream of the edge lip-line and along

the centerline. These locations are shown in Fig. 5. Results show a significant and consistent reduction of the velocity PSD in the case of porous 25 PPI along the centerline, as expected from the $-\overline{u'u'}/U_\infty^2$ and $-\overline{v'v'}/U_\infty^2$ results. A broadband peak is obvious at St=0.5 for porous 25 PPI, as shown at the near wake (P_1, W_1). This likely phenomena can also be seen in the boundary layer power spectra (Fig. 7(BP_{1-3}, BL_4)). The evolution of these broadband peak in the boundary layer and in the near wake of the shear layer is due to the pairing of the vortical structures, forming large coherent structures in the flow. Also, it is believed that there is an increase of the mixing layer thickness due to the velocity overshoot from the blunt trailing edge. However, as the measurement location moves downstream, this broadband peak disappears and consequently, the energy of these eddies decay further downstream.

The delayed vortex shedding build-up is also observed in these plots. The spectra given by the porous materials are getting closer and closer to the baseline case as moving downstream. The presence of the vortex shedding is distinctly pronounced with the appearance of several tonal peak values in the spectra. The amplitude of these peaks are reduced by both porous material, and the 25 PPI treatment also eliminates the peaks in the early wake. These tonal structures still build up in the farther wake in the 25 PPI case, but peaks with higher frequencies do not develop. In the upper plots, the similar peaks and its harmonics (at St=0.2 and St=0.4, respectively) are building up and for the porous 80 PPI, the peaks reached upon the baseline values in the farther downstream locations. The spectra velocity gradient shown in the plots appears close to the slope with $f^{-5/3}$. The slope subsequently deviates as the energy is dissipated throughout the time. Hence, it is affirmed that the amount of corresponding eddies is less for both porous cases relative to the solid one.

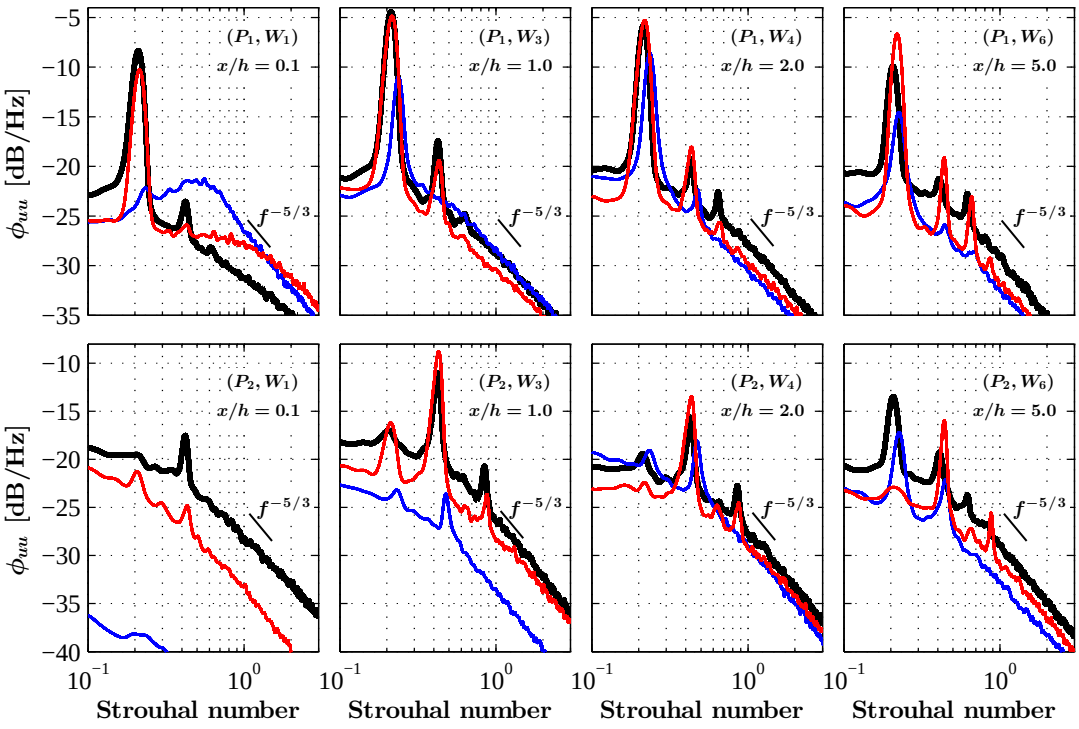

Figure 11: The power spectral density of the U velocity components at different locations in the wake. *Black line: Solid; Blue line: Porous 25 PPI; Red line: Porous 80 PPI.*

4. Power Spectra Contour Plots

Figure 12 shows the power spectra contour plots of the U velocity components for solid trailing edge at different x/h locations within the wake. It can be seen that the energy is mainly confined within the wake area, and the same tones can be found in these spectra as before. This means that high energy content is

experienced at St=0.2 and its harmonics. The hydrodynamic energy at St=0.2 can be felt well beyond the wake region, *i.e.* $y/h > 1.0$.

Figures 13 and 14 on the other hand present the PSD contour plots for porous 80 PPI and porous 25 PPI ϕ_{uu} components, normalized with the results obtained from the solid trailing edge, *i.e.* $(\phi_{uu})_{porous}$-$(\phi_{uu})_{solid}$. These figures help to identify the locations at which energy reduction or increase occurs in the wake area. It is clearly visible that the energy is reduced mainly at higher frequency region in the near wake by the 80 PPI material, and the energy is almost uniformly reduced at all scales in the case of the 25 PPI material. The reduction about the y axis at about St=0.2 and St=0.4 for both porous cases is due to the slight shift of the tonal peaks, as observed in the power spectral density of the U velocity components in Fig. 11. It is also visible that the energy content in Fig. 14 at x/h=0.1 increases significantly which is in agreement with the spectral broadband peak appear in the case of porous 25 PPI observed at (P_1, W_1). However, the energy content is consistently reduced in the downstream locations. It is also apparent that the hydrodynamic energy beyond the wake region, *i.e.* $y/h > 1.0$ of the trailing edge width shows significant reduction. It is clear that the energy is reduced significantly in the centerline and the shear layer by the 25 PPI material at all locations. These suggest that the use of porous TE has led to the removal of the vortex shedding from the near wake.

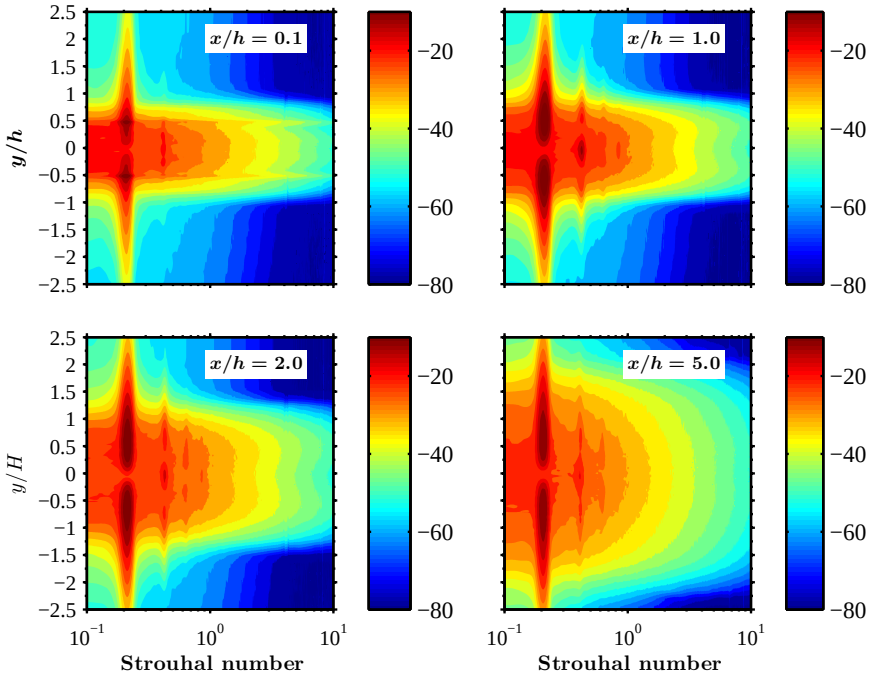

Figure 12: Contour plot of the solid blunt trailing edge power spectra for the U velocity component, ϕ_{uu}

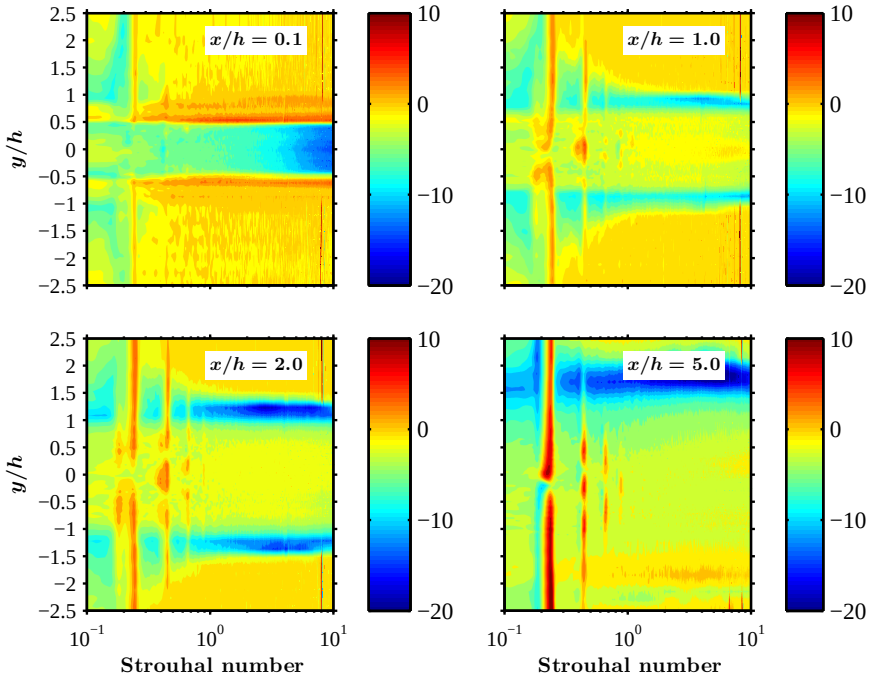

Figure 13: Contour plot of the reduction in the power spectra for the U velocity component for the 80 PPI porous material, $(\phi_{uu})_{porous80\ PPI}$-$(\phi_{uu})_{solid}$

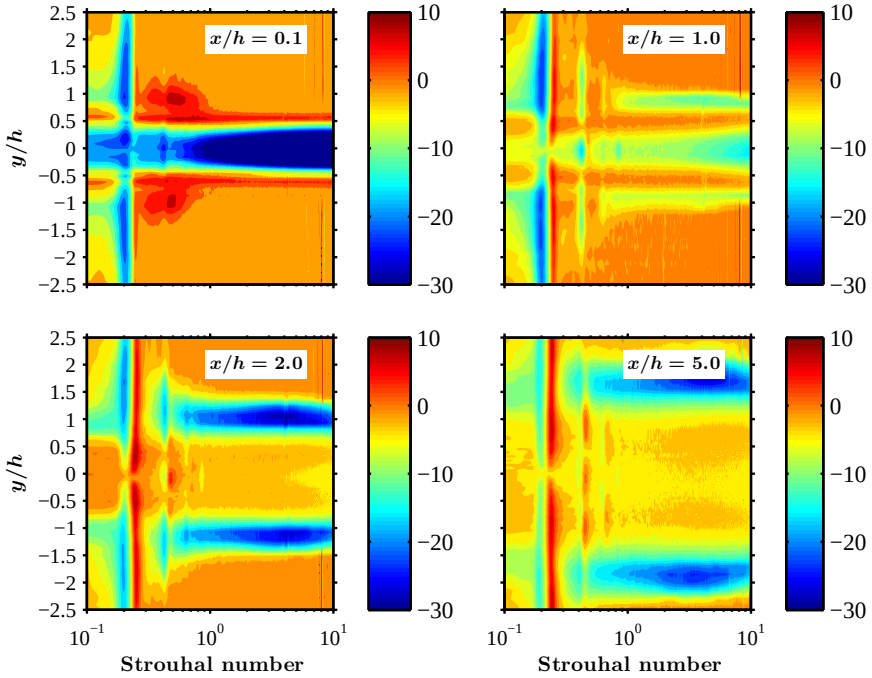

Figure 14: Contour plot of the reduction in the power spectra for the U velocity component for the 25 PPI porous material, $(\phi_{uu})_{porous25\ PPI}$-$(\phi_{uu})_{solid}$

E. Correlation Studies

The integral length scales have been calculated using the correlation data using Eqs. 11 and 12. The measurement have been performed using two hot-wire probes; one of the hot-wires has been fixed while the other one was traversed. The spanwise length scale measurements have been carried out at four different streamwise locations, $x/h = 0.5$ $x/h = 1.0$, $x/h = 2.0$ and $x/h = 3.0$. The streamwise length scale, on the other hand, has been performed by locating the fixed probe at $x/h = 0.1$, while the second probe was traversed up to $15h$ downstream of the edge lip-line of the upper trailing edge. The spanwise and streamwise integral length scales have been plotted as a function of the Strouhal number in Figs. 15 and 16, respectively.

In Fig. 15, it is obvious that the structure of the flow at different locations are slightly different. The solid and porous 80 PPI at $x/h = 0.5$ and $x/h = 1.0$ have a *dominant double peak* at the vortex shedding frequency. This double peak for solid case abide a *dominant peak* at St= 0.22 ($x/h = 0.5$ and 1.0) and a lower amplitude *secondary dominant peak* at a lower frequency at St= 0.19 ($x/h = 0.5$) and St= 0.2 ($x/h = 1.0$). The dominant double peak for the case of porous 80 PPI consists of a dominant peak at St= 0.22 ($x/h = 0.5$ and 1.0) and a lower amplitude secondary dominant peak at a lower frequency at St= 0.21 ($x/h = 0.5$ and 1.0). This variation of peak in the further downstream locations can only be seen in the case of porous 80 PPI. Besides, for the solid case, there is concurrent decrease in both the dominant peak and secondary dominant peak amplitude and becomes a single dominant peak in the later spanwise location. Moreau and Doolan[47] revealed that the multiple dominant peaks in the spectra are because of the cellular variation in spanwise vortex shedding frequency. The existence of dominant peak is due to the regular Karman vortex shedding at the trailing edge midspan. The secondary dominant peak on the other hand appeared due to a lower frequency shedding near the blunt TE-wall junction. It is anticipated that the reduction in the shedding frequency is due to the interaction between the Kármán vortices and the change in the downwash flow originating from the acceleration over the TE. It is of interest that the porous 25 PPI does not exhibits any dominant double peak. The 25 PPI material at $x/h = 0.5$ reduces the amplitude of the first peak, while reducing the integral length scale. Moving downstream, the 25 PPI material increases the amplitude of the rigid peak, eliminates the second peak while it increases the integral length scale uniformly in the region where the other materials show the second peak. It also can be seen that the harmonics develop for all cases at the further downstream.

The streamwise integral length scale can be seen in Fig. 16. The three cases show slightly different properties. The 80 PPI material reduces the size of the eddies, and the peaks are experienced approximately at the same Strouhal numbers. The 25 PPI material introduces a broadband increase in $L(f)$ while it decreases the main peak, and eliminates all the harmonics. Comparing the amplitude of dominant structures in the streamwise and spanwise directions for the corresponding materials, it can be deduced that for the solid case the spanwise direction of the eddies about the first peak ($x/h = 1.0$) is 3 times larger than in streamwise , for the 80 PPI case this number is slightly larger and finally for the 25 PPI material, the ratio is roughly the half of the baseline case. One can therefore infer that the use of porous materials has led to the elongation of the turbulent structures in spanwise direction in the near wake region, which also leads to the significant reduction in the energy content.

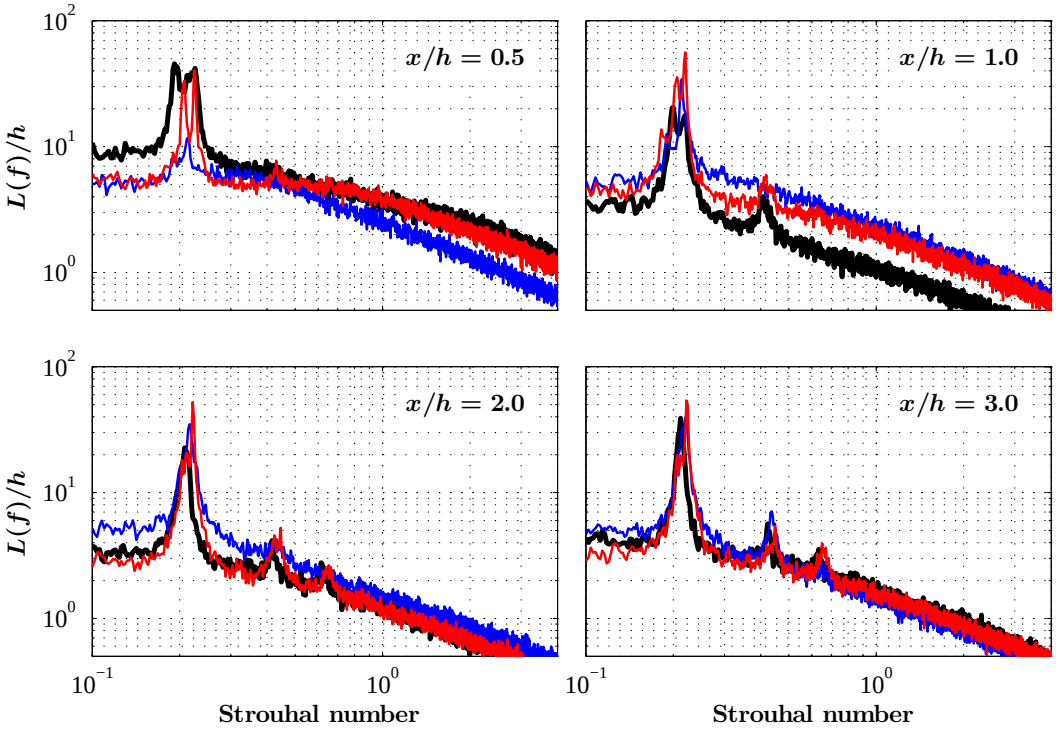

Figure 15: U velocity spanwise integral length scales at different x/h locations. *Black line: Solid; Blue line: Porous 25 PPI; Red line: Porous 80 PPI.*

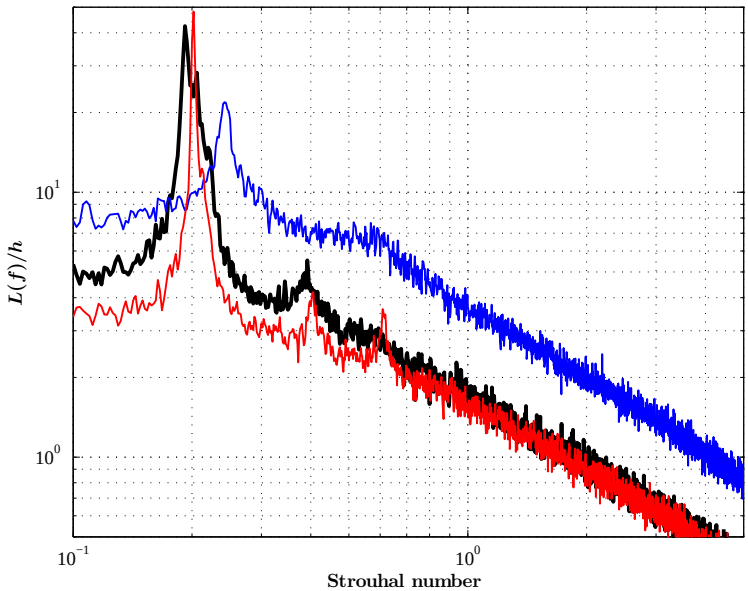

Figure 16: Streamwise integral length scales from x/h=0.1. *Black line: Solid; Blue line: Porous 25 PPI; Red line: Porous 80 PPI.*

V. Conclusions

The aerodynamics and aeroacoustics of the flow around a blunt trailing edge has been addressed and several measurements have been carried out at the open jet wind tunnel of the University of Bristol. The effect of applying porous treatments at the trailing edge have been widely investigated by single and cross hot-wire measurements, force balance measurements and boundary layer surface pressure measurements. It was found that the 25 PPI material yields to consistent drag reduction for all flow speeds, while the 80 PPI gave less significant drag reduction as the flow speed increased. It is also shown that the porous material are capable of reducing the acceleration of the flow in the boundary layer upstream of the trailing edge. The power spectra showed that significant reduction was achieved in the wake, and at the tonal behaviour of the vortices. It is also obvious that the porous treatment has noticeably modified the correlation length scale of the velocity fluctuations in both the spanwise and streamwise directions. Thus, the application of porous blunt trailing edge was found to be useful and effective in improving the aerodynamic performance and controlling the noise generation mechanism.

Acknowledgments

This project is sponsored by Embraer S.A. . The third author (MA) would like to acknowledge the financial support of the Royal Academy of Engineering.

References

[1]Lyu, B., Azarpeyvand, M., and Sinayoko, S., "Prediction of noise from serrated trailing edges," *Journal of Fluid Mechanics*, Vol. 793, 4 2016, pp. 556–588.

[2]Gruber, M., Azarpeyvand, M., and Joseph, P. F., "Airfoil trailing edge noise reduction by the introduction of sawtooth and slitted trailing edge geometries," *integration*, Vol. 10, 2010, pp. 6.

[3]Azarpeyvand, M., Gruber, M., and Joseph, P. F., "An analytical investigation of trailing edge noise reduction using novel serrations," *19th AIAA/CEAS Aeroacoustic Conference*, 2013, pp. 27–29.

[4]Sinayoko, S., Azarpeyvand, M., and Lyu, B., "Trailing edge noise prediction for rotating serrated blades," *20th AIAA/CEAS Aeroacoustics Conference*, 2014, pp. 16–20.

[5]Liu, X., Azarpeyvand, M., and Theunissen, R., "Aerodynamic and Aeroacoustic Performance of Serrated Airfoils," *21st AIAA/CEAS Aeroacoustics Conference*, 2015, p. 2201.

[6]Lim, H.-C. and Lee, S.-J., "Flow control of a circular cylinder with O-rings," *Fluid Dynamics Research*, Vol. 35, No. 2, 2004, pp. 107–122.

[7]Bearman, P. and Harvey, J., "Control of circular cylinder flow by the use of dimples," *AIAA journal*, Vol. 31, No. 10, 1993, pp. 1753–1756.

[8]Lim, H.-C. and Lee, S.-J., "Flow control of circular cylinders with longitudinal grooved surfaces," *AIAA journal*, Vol. 40, No. 10, 2002, pp. 2027–2036.

[9]Akilli, H., Sahin, B., and Tumen, N. F., "Suppression of vortex shedding of circular cylinder in shallow water by a splitter plate," *Flow Measurement and Instrumentation*, Vol. 16, No. 4, 2005, pp. 211–219.

[10]Ozono, S., "Flow control of vortex shedding by a short splitter plate asymmetrically arranged downstream of a cylinder," *Physics of Fluids*, Vol. 11, 1999, pp. 2928–2934.

[11]Ai, Q., Azarpeyvand, M., Lachenal, X., and Weaver, P. M., "Aerodynamic and aeroacoustic performance of airfoils with morphing structures," *Wind Energy*, 2015.

[12]Ai, Q., Weaver, P., and Azarpeyvand, M., "Design optimization of a morphing flap device using variable stiffness materials," *24th AIAA/AHS Adaptive Structures Conference*, 2016, p. 0816.

[13]Liu, H., Azarpeyvand, M., Wei, J., and Qu, Z., "Tandem cylinder aerodynamic sound control using porous coating," *Journal of Sound and Vibration*, Vol. 334, 2015, pp. 190–201.

[14]Liu, H., Wei, J., and Qu, Z., "The Interaction of Porous Material Coating With the Near Wake of Bluff Body," *Journal of Fluids Engineering*, Vol. 136, No. 2, 2014, pp. 021302.

[15]Liu, H., Wei, J., and Qu, Z., "Prediction of aerodynamic noise reduction by using open-cell metal foam," *Journal of Sound and Vibration*, Vol. 331, No. 7, 2012, pp. 1483–1497.

[16]Khorrami, M. R. and Choudhari, M. M., "Application of passive porous treatment to slat trailing edge noise," *NASA/TM*, Vol. 212416, 2003, pp. 2003.

[17]Bearman, P. W. and Tombazis, N., "The effects of three-dimensional imposed disturbances on bluff body near wake flows," *Journal of Wind Engineering and Industrial Aerodynamics*, Vol. 49, No. 1, 1993, pp. 339–349.

[18]Tombazis, N. and Bearman, P., "A study of three-dimensional aspects of vortex shedding from a bluff body with a mild geometric disturbance," *Journal of Fluid Mechanics*, Vol. 330, 1997, pp. 85–112.

[19]KJ., S. and van Dam CP, "Aerodynamic Analysis of Blunt Trailing Edge Airfoils," *Journal of Solar Energy Engineering / Volume 125 / Issue 4 / TECHNICAL PAPERS*, 2003.

[20]Hoerner, S. F. and Borst, H. V., "Fluid-dynamic lift: practical information on aerodynamic and hydrodynamic lift," 1985.

[21]Sato, J. and Sunada, Y., "Experimental research on blunt trailing-edge airfoil sections at low Reynolds numbers," *AIAA journal*, Vol. 33, No. 11, 1995, pp. 2001–2005.

[22]Deshpande, P. and Sharma, S., "Spanwise vortex dislocation in the wake of segmented blunt trailing edge," *Journal of Fluids and Structures*, Vol. 34, 2012, pp. 202–217.

[23]Nati, G., Kotsonis, M., Ghaemi, S., and Scarano, F., "Control of vortex shedding from a blunt trailing edge using plasma actuators," *Experimental Thermal and Fluid Science*, Vol. 46, 2013, pp. 199–210.

[24]Bruneau, C.-H., Mortazavi, I., and Gilliéron, P., "Flow regularisation and drag reduction around blunt bodies using porous devices," *IUTAM Symposium on Flow Control and MEMS*, Springer, 2008, pp. 405–408.

[25]Bae, Y., Jeong, Y. E., and Moon, Y. J., "Effect of porous surface on the flat plate self-noise," *Proceedings of the 15th AIAA/CEAS Aeroacoustics Conference, AIAA-Paper*, No. 2009-3311, 2009.

[26]Bae, Y. and Moon, Y. J., "Effect of passive porous surface on the trailing-edge noise," *Physics of Fluids (1994-present)*, Vol. 23, No. 12, 2011, pp. 126101.

[27]Schulze, J. and Sesterhenn, J., "Optimal distribution of porous media to reduce trailing edge noise," *Computers & Fluids*, Vol. 78, 2013, pp. 41–53.

[28]Zhou, B. Y., Gauger, N. R., Koh, S. R., Meinke, M., and Schröder, W., "Adjoint-based Trailing-Edge Noise Minimization using Porous Material," .

[29]Koh, S. R., Meinke, M., Schröder, W., Zhou, B., and Gauger, N., "Noise Sources of Trailing-Edge Turbulence Contolled by Porous Media," .

[30]Rae, W. H. and Pope, A., *Low-speed wind tunnel testing*, John Wiley, 1984.

[31]Blake, W. K., *Mechanics of Flow-Induced Sound and Vibration V2: Complex Flow-Structure Interactions*, Vol. 2, Elsevier, 2012.

[32]Schlichting, H., Gersten, K., and Gersten, K., *Boundary-layer theory*, Springer Science & Business Media, 2000.

[33]A/S, D. D., *Dantec Dynamics StreamWare Pro Installation and User Guide*, 5.11.00.14., 9040U4931, 2013.

[34]Garcia-Sagrado, A. and Hynes, T., "Wall pressure sources near an airfoil trailing edge under turbulent boundary layers," *Journal of Fluids and Structures*, Vol. 30, 2012, pp. 3–34.

[35]Gruber, M., *Airfoil noise reduction by edge treatments*, Ph.D. thesis, University of Southampton, 2012.

[36]Bull, M. and Thomas, A., "High frequency wall-pressure fluctuations in turbulent boundary layers," *Physics of Fluids (1958-1988)*, Vol. 19, No. 4, 1976, pp. 597–599.

[37]Bull, M., "Wall-pressure fluctuations beneath turbulent boundary layers: some reflections on forty years of research," *Journal of Sound and Vibration*, Vol. 190, No. 3, 1996, pp. 299–315.

[38]Goody, M. C. and Simpson, R. L., "An experimental investigation of pressure fluctuations in three-dimensional turbulent boundary layers," Tech. rep., DTIC Document, 1999.

[39]Brooks, T. F. and Hodgson, T., "Trailing edge noise prediction from measured surface pressures," *Journal of sound and vibration*, Vol. 78, No. 1, 1981, pp. 69–117.

[40]Williams, J. F. and Hall, L., "Aerodynamic sound generation by turbulent flow in the vicinity of a scattering half plane," *Journal of Fluid Mechanics*, Vol. 40, No. 04, 1970, pp. 657–670.

[41]Pope, S. B., *Turbulent flows*, Cambridge university press, 2000.

[42]AKERNATHY, F. H., "Fundamentals of boundary layers," 1988.

[43]Perry, A. and Marušic, I., "A wall-wake model for the turbulence structure of boundary layers. Part 1. Extension of the attached eddy hypothesis," *Journal of Fluid Mechanics*, Vol. 298, 1995, pp. 361–388.

[44]Taylor, G., "Flow in pipes and between parallel planes," *Proceedings of the Royal Society of London. Series A, Mathematical and Physical Sciences*, 1937, pp. 496–506.

[45]Lim, H.-C. and Lee, S.-J., "Flow control of a circular cylinder with O-rings," *Fluid Dynamics Research*, Vol. 35, No. 2, 2004, pp. 107–122.

[46]Bevilaqua, P. M., "Intermittency, the entrainment problem," 1973.

[47]Moreau, D. J. and Doolan, C. J., "Flow-induced sound of wall-mounted finite length cylinders," *AIAA journal*, Vol. 51, No. 10, 2013, pp. 2493–2502.